

Numerical Research on the Cold Start-up Strategy of a PEMFC Stack from -30°C

LEI Le, HE Pu, HE Peng, TAO Wen-quan*

Shaanxi Collaborative Innovation Center for PEMFC Performance Improvement, Key Laboratory of Thermal Fluid Science and Engineering of MOE, School of Energy and Power Engineering, Xi'an Jiaotong University, Xi'an 710049, China

© Science Press, Institute of Engineering Thermophysics, CAS and Springer-Verlag GmbH Germany, part of Springer Nature 2022

Abstract: The cold start-up of the PEMFC (proton exchange membrane fuel cell) stack from sub-zero temperature is considered one of the significant obstacles to its expansive commercial applications. In the cold start-up process, with the progress of hydrogen/oxygen chemical reaction, the produced water will freeze into ice, occupying the pores of the porous electrode, thus leading to a rapid deterioration of output performance and even making the cold start-up fail. In this work, a one-dimensional numerical model is adopted to study a cold start-up process of the PEMFC stack starting from -30°C . The stepwise-changed current loading mode is employed in the process. An assisted preheating method is used to explore an optimal operating condition for a successful cold start-up. The numerical results are validated by comparing the numerical result with the experimental data in reference, and they agree with the experimental data very well. The results show that the optimal heating power in the studied range is 100 W. As the initial current slope increased, the current peak value increased, but the cold start-up process failed. Also, the start-up time and ice volume fraction are highly dependent on the initial current slope. The optimal initial current slope is 0.7 A/s. Besides, a higher initial current slope will cause a significant inner ohmic resistance. The resistance of CLa (catalyst layer of the anode) is the key and primary part of the total ohmic resistance. The details of the research and the analyzed results will help design the cold start-up strategy for the PEMFC stack start-up from -30°C .

Keywords: cold start-up, PEMFC stack, stepwise-changed current loading mode, preheating

1. Introduction

Proton exchange membrane fuel cell (PEMFC) is regarded to be an effective alternative as a power plant for the automobile due to the attractive advantages [1–3] of high efficiency, low noise, and environment friendly. However, there is a challenge for the PEMFC start-up to

overcome in the sub-freezing temperature in winter [4]. In the sub-zero weather, the product water of the hydrogen/oxygen chemical reaction will freeze into ice, thus occupying the pores of the porous electrolyte [5–7]. Then, the output performance of the PEMFC remarkably deteriorates, finally, making the PEMFC shut down. Hence, the cold start-up under a sub-freezing temperature

Nomenclature

A	effective activation area/m ²	BP	bipolar plate
a	water activity	c	cathode
ASR	area-specific resistance/ $\Omega \cdot \text{m}^2$	cell	cell characteristic
C	mole concentration/mol·m ⁻³	CL	catalyst
c_{nfm}	mole concentration of the none-frozen membrane water/mol·m ⁻³	conc	concentration
c_p	specific heat capacity/J·kg ⁻¹ ·K ⁻¹	cond	condensation process
D	diffusivity/m ² ·s ⁻¹	cycle	the time cycle of the current loading
EW	the equivalent weight of membrane/kg·mol ⁻¹	eff	effective
F	Faraday's constant/C·mol ⁻¹	eq	equilibrium
h	convective heat transfer coefficient/W·m ⁻² ·K ⁻¹	evap	evaporation process
I	current/A	fl	fluid phase
j	exchange current density/A·cm ⁻²	fm	frozen membrane water
K	permeability/m ²	fusn	frozen
k	thermal conductivity/W·m ⁻¹ ·K ⁻¹	g	gas phase
M	molecular weight/kg·mol ⁻¹	GDL	gas diffusion layer
n	number of the current loading cycle	H ₂ O	water
p	pressure/Pa	i	the i th phase of water
Q	quantity of generated heat/J·cm ⁻²	ice	ice
R	universal gas constant/J·mol ⁻¹ ·K ⁻¹	j	the j th phase of water
S	mass/energy sources terms	l-i;	phase change between liquid and ice;
s	volume fraction	l-v	between liquid and vapor
t	time/s	load	current loading
T	temperature/K	lq	liquid water
V	the output voltage/V	mem	membrane
X	mass fraction of the vapor	nernst	nernst
Greek letters			
α	current loading slope	melt	represent the melting process
γ	water transfer rate	N	the freezing temperature
δ	thickness/mm	n-f;	phase change between non-frozen
ε	porosity	n-v;	and frozen; between non-frozen and
ζ	water transfer rate/s ⁻¹	n-i	vapor; between non-frozen and ice
κ	intrinsic permeability/m ²	nfm	none-frozen membrane water
λ	water content	ohmic	ohmic
μ	dynamic viscosity/kg·m ⁻¹ ·s ⁻¹	out	output
ξ	stoichiometry ratio	P	power
ρ	density/kg·m ⁻³	PC	phase change
σ	electric conductivity/S·m ⁻¹	sat	saturation
ω	the volume fraction of ionomer	sl	solid phase
Subscripts and superscripts			
a	anode	stack	stack characteristic
act	activation	T	energy (source term)
		vp	vapor
		wall	surrounding wall of the stack

is a significant obstacle for the PEMFC wide commercial applications on vehicles or other transports [8, 9].

In recent years, obtaining a successful cold start-up process with an optimal start-up strategy under sub-freezing temperatures tends to be interesting as the significant PEMFC research work. Many kinds of cold

start-up strategy works have been reported in the literature [10–13]. The cold start-up strategy is divided into two aspects [4, 14]. One is a self-heating start-up using the heat source of the electrochemical reaction, and another is assisted start-up with the external heat source. The common self-heating control approach in a cold

start-up process is the constant voltage mode, constant current mode, and constant power mode [15–17]. Luo et al. [16] conducted a one-dimensional stack model to elucidate and compare the constant power, voltage, and current cold start modes. The results showed that the constant power mode with a low current produces less heating than the other start-up modes. Yang et al. [17] experimentally studied the cold start-up process by the constant voltage mode to find the optimal operating conditions in a single cell. Besides, ramping and real-time adaptive modes [13, 18, 19] are also adopted in the start-up process. Jiang et al. [10] proposed a linear class current ramping protocol for a rapid cold start, and found that a small initial current density combined with an intermediate ramping rate and a large initial current density combined with a high ramping rate can obtain a successful cold start-up.

At some times, the self-heating is insufficient to warm up the PEMFC stack. Thus an assisted-heating [4] cold start-up strategy must be performed. Luo et al. [20] developed a hydrogen-oxygen catalytic reaction-assisted cold start method and utilized it with various start-up modes. The results showed that a high current operating way with a high air mole fraction is optimal and time-efficient. Recently, Yang et al. [21] conducted a transient system model, and then several assisted strategies, such as gas heating and coolant heating, were analyzed and compared. They found the power consumption for heating coolant is substantial, and secondary power sources are necessary.

Although an assisted-heating strategy can lead to a successful cold start-up process, it is usually used at a significantly lower temperature due to the requirements of secondary power sources. There are rarely self-heating strategies to get a successful start-up at the temperature of -30°C in the published literature. Therefore, the cold start at -30°C with the assisted-heating method still needs to

be focused on to get a proper and optimal strategy for a successful start-up. In this work, a one-dimensional numerical model of the PEMFC stack is adopted to explore the successful start-up operating conditions based on the pre-heating method with a stepwise-changed current loading mode at the temperature of -30°C .

2. Physical and Mathematical Model

The details of the adopted one-dimensional numerical model for the PEMFC stack cold start-up are depicted in this part.

2.1 Model description

Generally, a single PEMFC consists of the bipolar plate (BP), gas diffusion layer (GDL), microporous layer (MPL), and catalyst layer (CL) at both anode and cathode sides. A proton exchange membrane (MEM) is set in the central location. For the PEMFC stack, a series of single-cells are arranged with two endplates, current collectors on both sides of the stack. The schematic of the stack structure is shown in Fig. 1. The primary geometry parameters are illustrated in Table 1.

For a running PEMFC stack, a highly complex process occurs in real-time, such as fuel gas flow, hydrogen-oxygen chemical reaction, heat and mass transfer, and ion and electron transport. Numerical simulation for the cold start-up process of a PEMFC stack is a transient computation with a small time-step. Thus, using a three-dimensional model is almost prohibited. For this reason, the one-dimensional numerical stack model is adopted for the research of the cold start-up process in the references [21, 26, 27], and this practice is also adopted in this work. The limitation of the 1D model is that the in-plane distribution of parameters, such as temperature and membrane water, cannot be shown. The primary physical and chemical processes are only

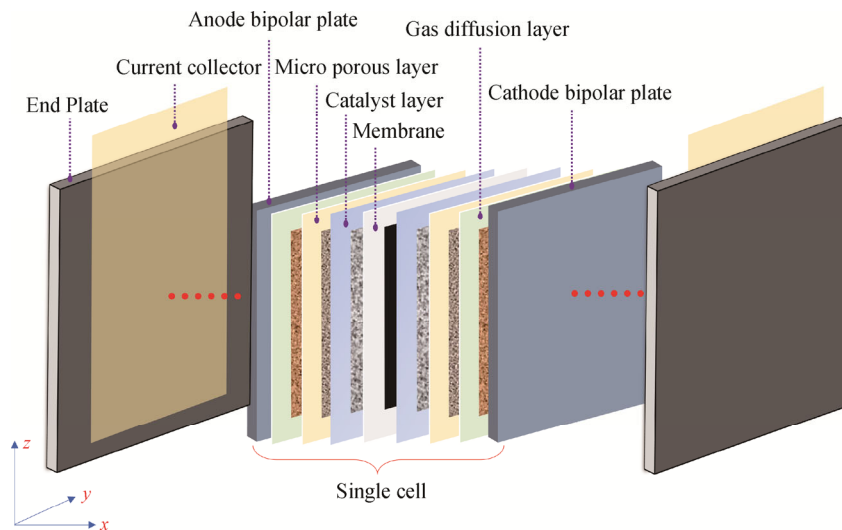


Fig. 1 Schematic of the structure of the PEMFC stack

Table 1 Geometry and physical parameters of the PEMFC stack

Physical parameters	Value	Unit
The active area of the cell [22]	25	cm ²
Thickness of BP; Channel; GDL; MPL; CL; membrane [23]	2000; 1000; 200; 30; 10; 30	μm
Porosities of GDL; MPL; CL [23]	0.7; 0.4; 0.3	
Contact angle of GDL; MPL; CL [23]	120; 100; 100	°
Intrinsic permeability of GDL; MPL; CL [24]	6.2×10^{-12} ; 6.2×10^{-13} ; 6.2×10^{-13}	m ²
Physical parameters	Value	Unit
Electrical conductivities of BP; GDL; MPL; CL [25]	25000; 300; 300; 300	S·m ⁻¹
Thermal conductivities of BP; GDL; MPL; CL; mem [25]	20; 1.5; 1.2; 1.2; 0.95	W·m ⁻¹ ·K ⁻¹
The mass density of the BP; GDL; MPL; CL; mem [25]	1000; 1000; 1000; 1000; 1980	kg·m ⁻³
The equivalent weight of the membrane [25]	1100	kg·mol ⁻¹
The specific heat capacity of BP; GDL; MPL; CL; mem [25]	1580; 2000; 568; 3300; 833	J·kg ⁻¹ ·K ⁻¹

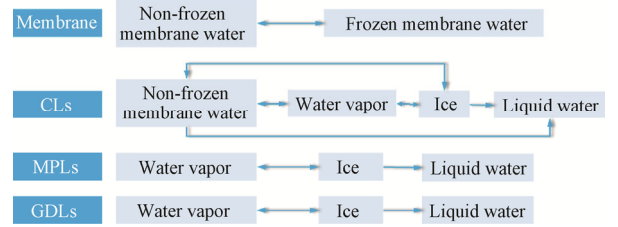
Table 2 Physical parameters and operating conditions of the model

Parameters	Value/Correction	Unit
Effective activation area	25	cm ²
Volume fraction of ionomer in CL	$\omega_a=0.23, \omega_c=0.23$	
Stoichiometry ratio	$ST_a=2.0, ST_c=3.0$	
Water transfer coefficient	$\gamma_a=0.5, \gamma_c=0.5$	
Initial stack temperature, T_{ini}	243.15	K
Pressure at outlets, p_{out}	101 325	Pa
Heat transfer coefficient on endplates surface, h	100.0	W·m ⁻² ·K ⁻¹
Initial non-frozen membrane water	6.2	
Phase change rate (ζ)	$\zeta_{i-l}=1.0, \zeta_{n-i}=2.5, \zeta_{n-l}=1.0, \zeta_{n-v}=2.5, \zeta_{n-t}=1.0$	s ⁻¹
Liquid water diffusivity [28]	$D_{lq} = -(K_{lq}/\mu_{lq})(dp_c/ds_{lq})$	m ² ·s ⁻¹
Capillary pressure in porous layers [29]	$\begin{cases} p_c = \sigma \cos(\theta)(\varepsilon/\kappa_0)^{0.5} [1.42(1-s_{lq}) - 2.12(1-s_{lq})^2 + 1.26(1-s_{lq})^3] & (\theta < 90^\circ) \\ p_c = \sigma \cos(\theta)(\varepsilon/\kappa_0)^{0.5} (1.42s_{lq} - 2.12s_{lq}^2 + 1.26s_{lq}^3) & (\theta > 90^\circ) \end{cases}$	Pa
Effective permeability of liquid water [28]	$\kappa_{lq} = \kappa_0 s_{ice}^{4.0} (1-s_{ice})^{4.0}$	m ²
Equivalent water content and water activity [30]	$\lambda_{eq} = \begin{cases} 0.043 + 17.81a - 39.58a^2 + 36.0a^3 & (0 \leq a < 1) \\ 14.0 + 1.4(a-1) & (1 < a \leq 3) \end{cases}$ $a = X_{vp} p_g / p_{sat} + 2s_{lq}$	
Effective volumetric heat capacities	$(\rho c_p)_{fl,sl}^{eff} = \varepsilon [s_{lq} \rho_{lq} (c_p)_{lq} + s_{ice} \rho_{ice} (c_p)_{ice} + (1-s_{lq}-s_{ice}) \rho_g (c_p)_g] + (1-\varepsilon-\omega) \rho_s (c_p)_s + \omega \rho_{mem} (c_p)_{mem}$	J·m ⁻³ ·K ⁻¹
Effective thermal conductivity	$k_{fl,sl}^{eff} = \varepsilon [s_{lq} k_{lq} + s_{ice} k_{ice} + (1-s_{lq}-s_{ice}) k_g] + (1-\varepsilon-\omega) k_s + \omega k_{mem}$	W·m ⁻¹ ·K ⁻¹

considered in the through-plane direction (x -direction, as shown in Fig. 1). For the cold start-up process study, the in-plane averaged parameters are sufficient.

There are phase-change processes in the CLs between the non-frozen membrane water, vapor, ice, and liquid water. In the MEM, under the amount of non-frozen membrane water reaches larger than the saturated membrane water, it will change into the frozen membrane water. The water vapor will move into MPLs and GDLs from the CLs and then be transformed into ice because of the diffusion process. When the temperature rises to 273.15 K, the ice will melt into liquid water.

The water transition mechanism is detailedly depicted in Fig. 2. It is worth claiming that the entire process is considered to be occurred at the cathode side due to a large amount of non-frozen membrane water existing in

**Fig. 2** Water transition mechanism of the model

CLc, while a relatively lower quantity in CLa. And mass governing equations are solved inside every cell, and then the energy conservation equation is solved with several source terms among the entire PEMFC stack.

Our preliminary computations have found that the pre-heating process only affects the two to three cells close to the bipolar plate on both sides of the PEMFC stack. Thus, to save the simulation time, we choose five cells.

Some physical and operating parameters in the one-dimensional numerical model are represented in

Table 2. The value or correction formulas are given precisely and then utilized in the after study of the cold start-up strategy.

2.2 Governing equations and output performance

The water states and energy transport processes are solved using the five mass conservation equations and an energy conservation equation. There are none-frozen membrane water, frozen membrane water, liquid water, water vapor, ice, and energy governing equations, respectively, as listed in Table 3.

Table 3 Governing equations

Terms	Equations
None-frozen membrane water	$\frac{\rho_{\text{mem}}}{\text{EW}} \cdot \frac{\partial(\omega\lambda_{\text{nfm}})}{\partial t} = \frac{\rho_{\text{mem}}}{\text{EW}} \cdot \frac{\partial^2(\omega^{1.5}D_{\text{nfm}}\lambda_{\text{nfm}})}{\partial x^2} + S_{\text{nfm}}$
Frozen membrane water	$\frac{\rho_{\text{mem}}}{\text{EW}} \cdot \frac{\partial(\omega\lambda_{\text{fm}})}{\partial t} = S_{\text{fm}}$
Liquid water	$\frac{\partial(\varepsilon\rho_{\text{liq}}s_{\text{liq}})}{\partial t} = \frac{\partial^2(\rho_{\text{liq}}D_{\text{liq}}s_{\text{liq}})}{\partial x^2} + S_{\text{liq}}$
Water vapor	$\frac{\partial(\varepsilon(1-s_{\text{liq}}-s_{\text{ice}})\rho_{\text{g}}c_{\text{vp}})}{\partial t} = \frac{\partial^2(\rho_{\text{g}}D_{\text{vp}}c_{\text{vp}})}{\partial x^2} + S_{\text{vp}}$
Ice	$\frac{\partial(\varepsilon\rho_{\text{ice}}s_{\text{ice}})}{\partial t} = S_{\text{ice}}$
Energy	$\frac{\partial}{\partial t}[(\rho c_p)_{\text{fl,sl}}^{\text{eff}} T] = \frac{\partial^2(k_{\text{fl,sl}}^{\text{eff}} T)}{\partial x^2} + S_{\text{T}}$
Output voltage	$V_{\text{out}} = V_{\text{nernst}} + V_{\text{act}} + V_{\text{conc}} + V_{\text{ohmic}}$
Activation voltage loss	$V_{\text{act}} = -\frac{RT}{\alpha F} \ln \left\{ \frac{I}{(1-s_{\text{ice}}-s_{\text{liq}})^{0.5} \cdot j \cdot \delta_{\text{CL}} \left[\frac{0.21 \cdot p_c \cdot [1+(1-1/\xi)]}{2RT \cdot c_{\text{ref}}} \right]} \right\}$
Ohmic voltage loss	$V_{\text{ohmic}} = -ASR \cdot j$
Concentration voltage loss	$V_{\text{conc}} = \frac{RT}{\alpha F} \ln \left(1 - \frac{I}{j_D} \right)$

The diffusion coefficient D_{nfm} in the governing equation of non-frozen membrane water is corrected by temperature and water content, as expressed in Eq. (1).

$$D_{\text{nfm}} = \begin{cases} 2.69266 \times 10^{-10} & \lambda_{\text{nfm}} \leq 2 \\ 10^{-10} \cdot \exp \left[2416 \left(\frac{1}{303} - \frac{1}{T} \right) \right] \cdot [0.87(3 - \lambda_{\text{nfm}}) + 2.95(\lambda_{\text{nfm}} - 2)] & 2 < \lambda_{\text{nfm}} \leq 3 \\ 10^{-10} \cdot \exp \left[2416 \left(\frac{1}{303} - \frac{1}{T} \right) \right] \cdot [2.95(4 - \lambda_{\text{nfm}}) + 1.642454(\lambda_{\text{nfm}} - 3)] & 3 < \lambda_{\text{nfm}} \leq 4 \\ 10^{-10} \cdot \exp \left[2416 \left(\frac{1}{303} - \frac{1}{T} \right) \right] \cdot (2.563 - 0.33\lambda_{\text{nfm}} + 0.0264\lambda_{\text{nfm}}^2 - 0.0006713\lambda_{\text{nfm}}^3) & \lambda_{\text{nfm}} > 4 \end{cases} \quad (1)$$

The output voltage is solved analytically by the Tafel representation [31] by considering the activation, concentration, and ohmic voltage loss (the correction formulas are presented in Table 3). As for the output voltage, V_{nernst} denotes the Nernst voltage, as expressed as Eq. (2).

$$V_{\text{nernst}} = 1.23 - 0.9 \times 10^{-3} \cdot (T - T_0) + \frac{RT_0}{2F} \ln \left(\frac{p_{\text{H}_2} \cdot p_{\text{O}_2}}{p_{\text{H}_2\text{O}}} \right) \quad (2)$$

ASR (Ω) in the ohmic voltage loss equation is the total area-specific resistance, calculated by Eq. (3).

$$\text{ASR} = A_{\text{cell}} \left(\frac{\delta_{\text{BP}}}{\sigma_{\text{BP}} A_{\text{cell}}} + \frac{\delta_{\text{GDL}}}{\sigma_{\text{GDL}} A_{\text{cell}}} + \frac{\delta_{\text{MPL}}}{\sigma_{\text{MPL}} A_{\text{cell}}} + \frac{\delta_{\text{CL}}}{\sigma_{\text{CL}} A_{\text{cell}}} + \frac{\delta_{\text{mem}}}{\sigma_{\text{mem}} A_{\text{cell}}} \right) \quad (3)$$

j_{D} in the concentration voltage loss equation is defined as

$$j_{\text{D}} = \frac{4F \cdot c_{\text{h}}}{\frac{\delta_{\text{GDL}}}{D_{\text{GDL}}^{\text{eff}}} + \frac{\delta_{\text{MPL}}}{D_{\text{MPL}}^{\text{eff}}} + 0.5 \frac{\delta_{\text{CL}}}{D_{\text{CL}}^{\text{eff}}}} \quad (4)$$

$$\lambda_{\text{sat}} = \begin{cases} 4.837 & (T < 223.15 \text{ K}) \\ \left(-1.304 + 0.014 \cdot 79T - 3.594 \times 10^{-5} T^2 \right)^{-1} & (223.15 \text{ K} \leq T < T_{\text{freeze}}) \\ > \lambda_{\text{nfmem}} & (T \geq T_{\text{freeze}}) \end{cases} \quad (7)$$

where σ_i denotes the electric conductivity; $D_{\text{GDL}}^{\text{eff}}$, $D_{\text{MPL}}^{\text{eff}}$ and $D_{\text{CL}}^{\text{eff}}$ are effective diffusivity of water vapor inside the GDL, MPL, and CL, respectively.

Source terms of the governing equations are summarized in Table 4. The source term of the electro-osmotic drag process is calculated as

$$S_{\text{EOD}} = \nabla \cdot \left(\frac{n_{\text{d}}}{F} \kappa_{\text{ion}}^{\text{eff}} \nabla \phi_{\text{ion}} \right) \quad (5)$$

where, $\nabla \phi_{\text{ion}}$ is the ionic potential and $\kappa_{\text{ion}}^{\text{eff}}$ is the effective ionic conductivity. n_{d} (number of the molecules dragged per hydrogen ion through the electrolyte) is the electro-osmotic drag coefficient and is highly related to the membrane water uptake of the MEM [32]:

$$n_{\text{d}} = 2.5 \lambda_{\text{nfmem}} / 22 \quad (6)$$

The phase change source terms of the five water states are detailedly illustrated in Table 5. λ_{sat} represents the saturated membrane water content, which determines the phase change process between non-frozen membrane water and frozen membrane water in MEM and the change process among non-frozen membrane water and ice. It is calculated by Eq. (7).

Table 4 Source terms of mass conservation equations

Terms	Expression	Unit
Non-frozen membrane water	$S_{\text{nfmem}} = \begin{cases} -S_{\text{n-f}} & \text{(in membrane)} \\ \frac{j_{\text{e}}}{2F} - S_{\text{n-v}} - S_{\text{n-i}} + S_{\text{EOD}} & \text{(in cathode CL)} \\ -S_{\text{n-v}} - S_{\text{n-i}} + S_{\text{EOD}} & \text{(in anode CL)} \end{cases}$	$\text{kmol} \cdot \text{m}^{-3} \cdot \text{s}^{-1}$
Frozen membrane water	$S_{\text{fm}} = S_{\text{i-1}} + S_{\text{n-1}} M_{\text{H}_2\text{O}}$	$\text{kmol} \cdot \text{m}^{-3} \cdot \text{s}^{-1}$
Liquid water	$S_{\text{liq}} = S_{\text{v-1}} - S_{\text{l-1}}$	$\text{kg} \cdot \text{m}^{-3} \cdot \text{s}^{-1}$
Water vapor	$S_{\text{vp}} = \begin{cases} -S_{\text{v-1}} + S_{\text{n-v}} M_{\text{H}_2\text{O}} & \text{(in CL)} \\ -S_{\text{v-1}} & \text{(in GDL)} \end{cases}$	$\text{kg} \cdot \text{m}^{-3} \cdot \text{s}^{-1}$
Ice	$S_{\text{ice}} = \begin{cases} S_{\text{l-1}} + S_{\text{n-1}} M_{\text{H}_2\text{O}} & \text{(in CL)} \\ S_{\text{l-1}} & \text{(in GDL)} \end{cases}$	$\text{kg} \cdot \text{m}^{-3} \cdot \text{s}^{-1}$
Energy	$S_{\text{T}} = \begin{cases} j_{\text{e}} \eta_{\text{act}} + \frac{I^2 \text{ASR}_{\text{CL}}}{3\delta_{\text{CL}}} + S_{\text{PC}} & \text{(in anode CL)} \\ -\frac{j_{\text{e}} T \Delta S}{2F} + j_{\text{e}} \eta_{\text{act}} + \frac{I^2 \text{ASR}_{\text{CL}}}{3\delta_{\text{CL}}} + S_{\text{PC}} & \text{(in cathode CL)} \\ \frac{I^2 \text{ASR}_{\text{GDL}}}{\delta_{\text{GDL}}} + S_{\text{PC}} & \text{(in GDL)} \\ \frac{I^2 \text{ASR}_{\text{BP}}}{\delta_{\text{BP}}} & \text{(in BP)} \\ \frac{I^2 \text{ASR}_{\text{mem}}}{\delta_{\text{mem}}} + S_{\text{PC}} & \text{(in membrane)} \end{cases}$	$\text{W} \cdot \text{m}^{-3}$

Table 5 Phase change source terms of water states [32]

Terms	Expression	Unit
Non-frozen membrane water \leftrightarrow frozen membrane water	$S_{n-f} = \begin{cases} \xi_{n-f} \frac{\rho_{\text{mem}}}{EW} (\lambda_{\text{nfim}} - \lambda_{\text{sat}}) & (\text{if } \lambda_{\text{nfim}} > \lambda_{\text{sat}}) \\ \xi_{n-f} \frac{\rho_{\text{mem}}}{EW} \lambda_{\text{nfim}} & (\text{if } \lambda_{\text{nfim}} < \lambda_{\text{sat}}) \end{cases}$	$\text{mol}\cdot\text{m}^{-3}\cdot\text{s}^{-1}$
Non-frozen membrane water \leftrightarrow water vapor	$S_{n-v} = \xi_{n-v} \frac{\rho_{\text{mem}}}{EW} (\lambda_{\text{nfim}} - \lambda_{\text{eq}}) (1 - s_{\text{liq}} - s_{\text{ice}})$	$\text{mol}\cdot\text{m}^{-3}\cdot\text{s}^{-1}$
Non-frozen membrane water \leftrightarrow ice	$S_{n-i} = \begin{cases} \xi_{n-i} \frac{\rho_{\text{mem}}}{EW} (\lambda_{\text{nfim}} - \lambda_{\text{sat}}) (1 - s_{\text{liq}} - s_{\text{ice}}) & (\text{if } \lambda_{\text{nfim}} > \lambda_{\text{sat}}) \\ 0 & (\text{if } \lambda_{\text{nfim}} < \lambda_{\text{sat}}) \end{cases}$	$\text{kg}\cdot\text{m}^{-3}\cdot\text{s}^{-1}$
Liquid water \leftrightarrow ice	$S_{l-i} = \begin{cases} \gamma_{\text{fust}} \varepsilon s_{\text{liq}} \rho_{\text{liq}} & (\text{if } T < T_N) \\ -\gamma_{\text{melt}} \varepsilon s_{\text{ice}} \rho_{\text{ice}} & (\text{if } T \geq T_N) \end{cases}$	$\text{kg}\cdot\text{m}^{-3}\cdot\text{s}^{-1}$
Water vapor \leftrightarrow liquid water	$S_{v-l} = \begin{cases} \gamma_{\text{cond}} \varepsilon (1 - s_{\text{liq}} - s_{\text{ice}}) \frac{(p_g X_{\text{vp}} - p_{\text{sat}}) M_{\text{H}_2\text{O}}}{RT} & (\text{if } p_g X_{\text{vp}} \geq p_{\text{sat}}) \\ \gamma_{\text{evap}} \varepsilon s_{\text{liq}} \frac{(p_g X_{\text{vp}} - p_{\text{sat}}) M_{\text{H}_2\text{O}}}{RT} & (\text{if } p_g X_{\text{vp}} < p_{\text{sat}}) \\ 0 & (\text{if } T < T_N) \end{cases}$	$\text{kg}\cdot\text{m}^{-3}\cdot\text{s}^{-1}$

2.3 Boundary and initial conditions

There is no ice in the porous zones initially, and the membrane water content is set as 6.2 [22] for a relatively lower initial inner resistance. The initial temperature of the stack is 243.15 K. According to our published paper [23], the time step is 0.1 s to get a highly time-efficiency simulation that can also guarantee the simulation's accuracy. The convective heat transfer boundary is set to both sides of the endplate surface, and the heating loss is calculated by

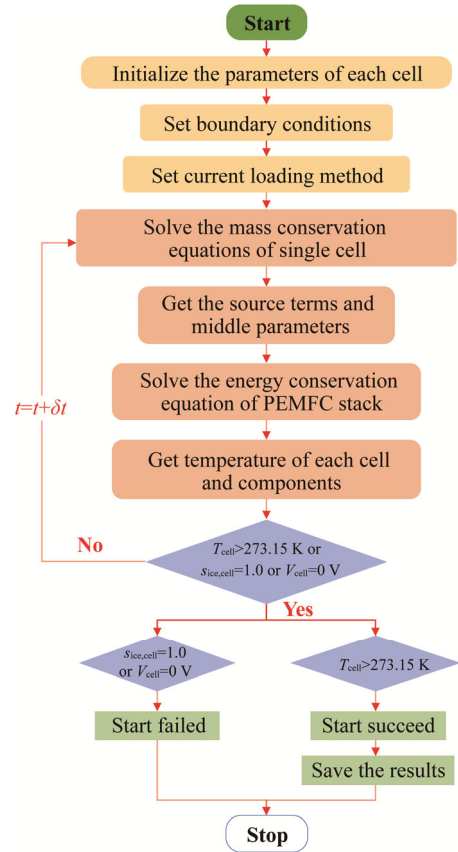
$$Q_{\text{loss}} = hA_{\text{cell}} (T_{\text{sur}} - T_{\text{wall}}) \quad (8)$$

where h is the heat transfer coefficient; T_{sur} is the ambient temperature, and set the value a constant of 243.15 K.

2.4 Simulation procedure

The one-dimensional model is coded in MATLAB software. Fig. 3 shows the calculation flow process. Before starting, the PEMFC stack is heated with a specific power for 30 s, wherein the heating pad is located between the current collector and BP. The current loading mode will be performed after the initialization. It is important to note that the mass conservation equations of each water state are solved in every cell, and thus the water distribution and various source terms can be obtained. The temperature distribution will be received in succession by solving the energy conservation equation in the entire stack region.

The present research studied the effects of pre-heating power and initial current loading slope on the cold start-up process. According to Refs. [16, 21, 33], if the maximum volume fraction of ice is more than one or the minimum output voltage is less than 0, the simulation

**Fig. 3** Calculation flow chart of the simulation model

process will shut down, which means the cold start-up process is failed. In contrast, if the temperature of every cell is larger than the freezing temperature, the cold start-up process is successful.

3. Results and Discussion

In this section, the optimal initial current loading slope and the heating power will be explored based on the above-mentioned numerical models and methods.

3.1 Model verification

The numerical model is validated by comparing the output cell voltage with the experimental data in Ref. [22]. Fig. 4 shows the comparison of the cell output voltage between the numerical result and the experimental data. The current loading method is the same as the experiment in the reference. The initial current ramp is $0.5 \text{ mA} \cdot \text{cm}^{-2} \cdot \text{s}^{-1}$ for 80 s, and then the current is set as a constant until the end of the start-up process. It can be seen that as the current rises, the output voltage decreases quickly, and the maximum error is 9.2% at the ramping stage. The numerical result agrees very well with the experimental data when the current is kept constant. At the end stage, the numerical data show a noticeable difference. This is a pervasive situation between numerical results and test data for the PEMFC cold-startup [24, 34] to the authors' knowledge. However, the start-up time is close to the experiment duration. Hence, the one-dimensional numerical model can be used in the following research cases.

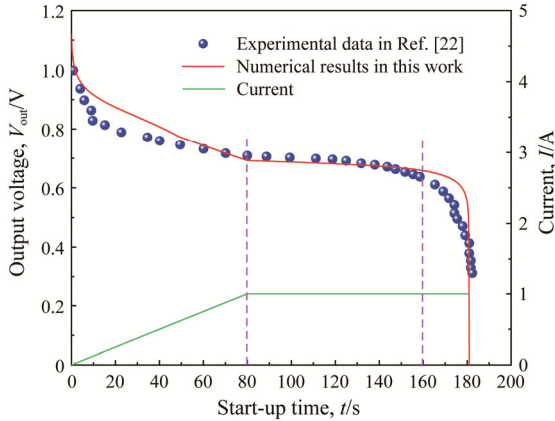


Fig. 4 Comparison between the numerical result and experimental data

3.2 Analysis of the simulation results

As been studied in our published work [23], the stepwise-changed current loading mode shows better output performance for a PEMFC cold start. Thus, in the present research, we study the PEMFC cold start under -30°C based on the current loading mode. Several slope values are designed to use in a cold start-up process of the PEMFC stack to get an optimal initial current ramping slope. The current loading strategy is detailedly illustrated in Fig. 5.

3.2.1 Determination of heating power

As mentioned in the first section, self-heating without external heating is unachievable for the PEMFC cold start-up from -30°C . Therefore, external power is adopted to help to heat the PEMFC stack before the current loading. To select a proper heating power, six different values of the heating power are utilized in the corresponding six PEMFC cold start-up processes. The initial current ramping slope is set as $1.0 \text{ A} \cdot \text{s}^{-1}$ in the six cases. The details of the cold start-up processes are shown in Table 6.

It can be found that, as the heating power increases, the start-up time tends to be decreased as well as the maximum ice volume fraction in the cathode catalyst layer. Simultaneously, the start-up process is failed when the heating power is less than 120 W. For the two failed cases, the maximum ice volume fraction is 1.0. Still, it gets a relatively lower temperature (the maximum temperature in the stack) than the successful start-up case (The heating power is 120 W). Considering the PEMFC stack is working with a temperature close to 80°C under a normal operation situation, a higher temperature will cause the membrane to dry out and degrade the PEMFC performance. Due to the heating pad being usually used to heat the stack until the end of the cold start-up, the temperature of the stack will rise continually during the entire start process. Hence the heating power must be small to obtain a lower temperature. When the heating power is 150 W, the cold start-up gets a successful procedure with a lower ice volume fraction and temperature, but the current is smaller than those in other cases.

Table 6 Details of the cold start-up processes under different heating power

Heating power, P/W	Start-up time, t/s	Succeed (S) or Failed (F)	The maximum temperature, T_{max}/K	The maximum ice volume fraction, $s_{\text{ice, max}}$	The maximum current, I_{max}/A
100	71.9	F	402	1.0	6.31
110	66.4	F	404	1.0	6.19
120	63.9	S	419	0.94	6.26
130	60.9	S	420	0.79	6.05
140	58.5	S	417	0.66	5.57
150	56.6	S	407	0.54	4.0

When the current value is the aim of the cold start-up strategy, the larger heating power is inapplicable for the cold start-up process.

The heating power is 100 W in the following research cases and then explores an optimal current loading strategy.

3.2.2 The influences of current ramping slope

Nine values are designed to conduct nine numerical simulation cases of the PEMFC cold start-up process to find an optimal initial current ramping slope. The initial conditions are the same except for the initial current ramping slope in all cases.

Fig. 5 shows the current value and average output voltage of the PEMFC stack. Fig. 5(a) shows that the current peak value increased during the cold start-up process as the initial current slope increased. Besides, when the slope is larger than $0.5 \text{ A}\cdot\text{s}^{-1}$, the current increasing trend will be slow after a rapidly growing stage, and then the current will decrease due to reaching the output voltage threshold for the current decreasing

stage. As shown in Fig. 5(b), the average output voltage is dropped more seriously with the increase of the initial current slope. When the rise of the current trend is slower, the output voltage decreases slightly until the sharply dropping process is in the final stage. We can find that the voltage will re-increase when the initial current slope is no more than $0.7 \text{ A}\cdot\text{s}^{-1}$.

The variation of the single-cell voltage during the cold start-up process is shown in Fig. 6. For the successful case, the initial current slope is $0.7 \text{ A}\cdot\text{s}^{-1}$. While, for the failed case, the initial current ramp is $0.8 \text{ A}\cdot\text{s}^{-1}$. It can be found that the output voltage of the cell changed to re-rise during the end-stage for the successful cold start-up process, while in the failed case, the voltage of the cell-3 dropped to zero, thus causing the cold start-up process to shut down. Therefore, the optimal initial current slope is $0.7 \text{ A}\cdot\text{s}^{-1}$. Besides, the voltage of cell-1 and cell-5 decreases during the end-stage because the activation voltage loss increases with the temperature rising.

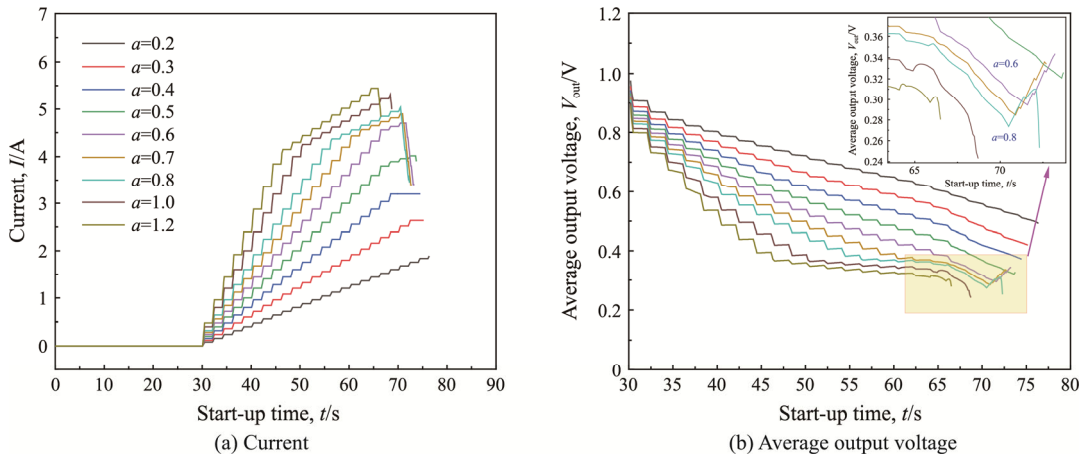


Fig. 5 Current and output voltage under the different initial current slope

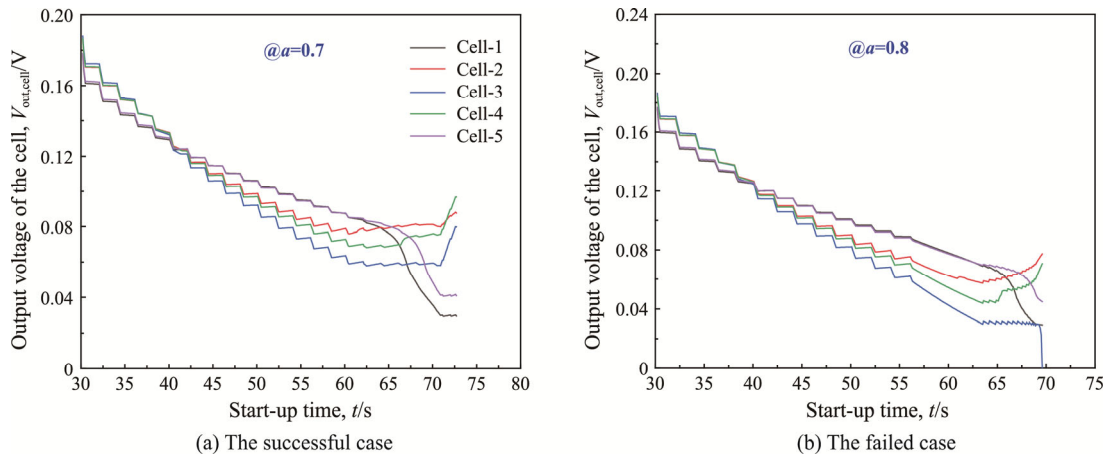


Fig. 6 Output cell voltage for a successful and a failed case

Fig. 7 shows the average ice volume fraction in the cathode under the different initial current slopes. During the pre-heating stage, there no ice is formed. While, when the current is loading, the ice volume fraction is quickly increasing. Obviously, the volume fraction of the ice is closely related to the current. As the current decreases at the end-stage, it also decreases. The higher initial current slope causes a large amount of ice. It is disadvantageous to the fuel gas diffusion in the pores of the porous electrolyte and thus gets a higher concentration voltage loss.

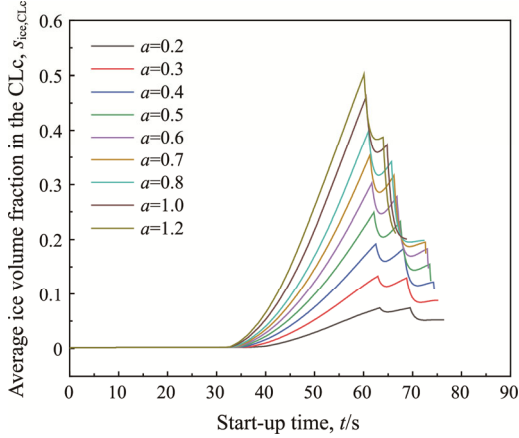


Fig. 7 Average ice volume fraction in the CLc under the different initial current slope

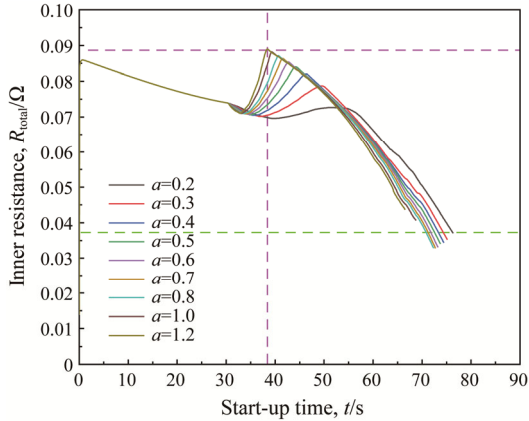
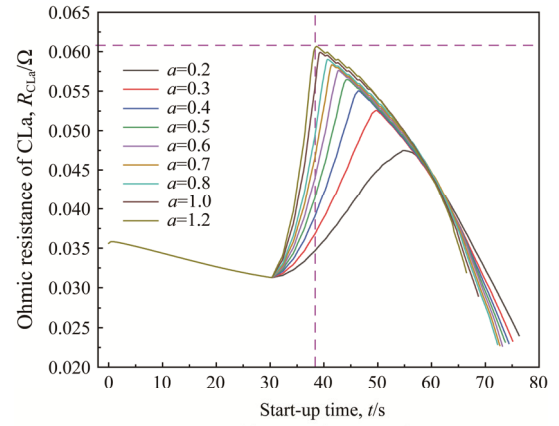


Fig. 8 Inner ohmic resistance under the different initial current slope

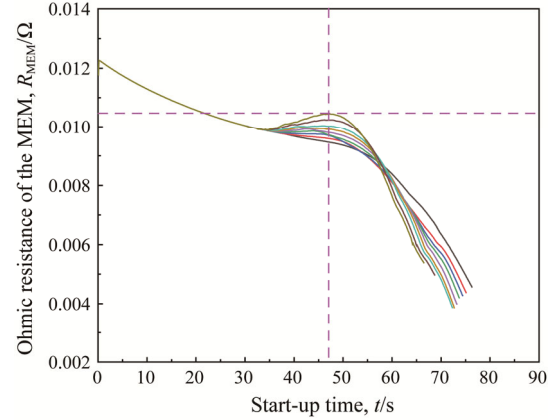
The average inner ohmic resistance of the stack under the different initial current slopes is shown in Fig. 8. The ohmic resistance is 85 mΩ with the initial membrane water content set as 6.2 as suitable at the initial time. In the pre-heating stage, the resistance decreases, and this is because the temperature increases and then causes the rise in ionic conductivity. When the current is starting to be loaded, the ohmic resistance decreases slightly and then increases sharply to the peak value, then reduces with start-up time. The peak value of the resistance is growing with the initial current slope. For the successful

cold start-up processes ($\alpha < 0.8 \text{ A}\cdot\text{s}^{-1}$), the final ohmic resistance is lower than 38 mΩ.

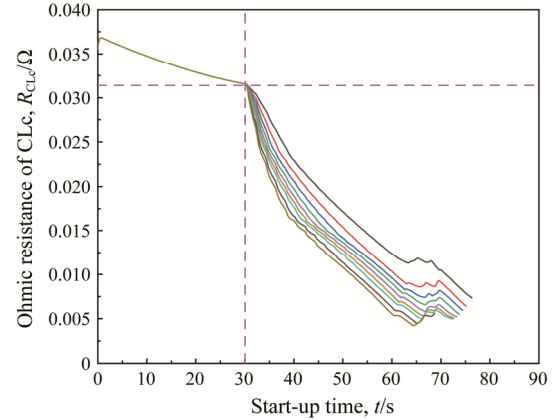
Fig. 9 demonstrates the inner resistance of the PEMFC assembly components. The resistance of the CLa and MEM increases when the current is loading during the initial loading time (after 30 s). This is caused by the electro-osmotic drag process resulting in the membrane water content reduction in the CLa and MEM. As the current increases to a higher value, the amount of membrane water in the CLc becomes more extensive, thus enhancing the membrane water diffusion process.



(a) Ohmic resistance of CLa



(b) Ohmic resistance of MEM



(c) Ohmic resistance of CLc

Fig. 9 Inner resistance of the PEMFC assembly components

Hence, the membrane water content in the CLa and MEM tends to increase and increase the ionic conductivity, then reduce the resistance. While the resistance for the CLc decreases prominently during the start-up time except for the pre-heating time. It is worth noting that the percentage of the resistance in the CLa, MEM, and CLc are almost 70%, 20%, and 10%, respectively.

The average temperature of the stack is shown in Fig. 10. At the pre-heating time, the temperature rises with a nearly linear tendency. The effects of the initial current slope on the temperature tend to be significant during the end-stage: the temperature increases when the current slope is close to the optimal value ($0.7 \text{ A}\cdot\text{s}^{-1}$). Fig. 11 shows the variation of the single-cell temperature with time, in which the initial current slope is $0.7 \text{ A}\cdot\text{s}^{-1}$. It can be found that the temperature of the middle cell (cell-3) is challenging to rise, while the cells located on both sides of the stack have a higher temperature.

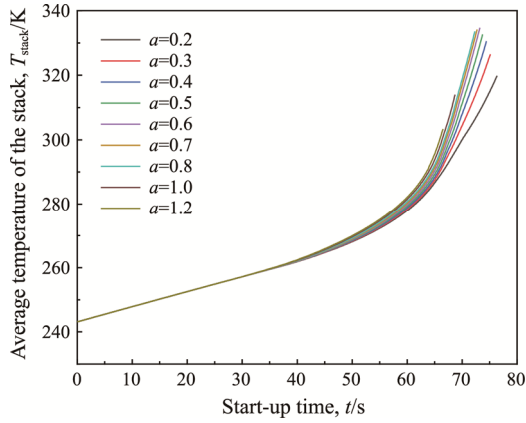


Fig. 10 Average temperature of the stack under the different initial current ramp

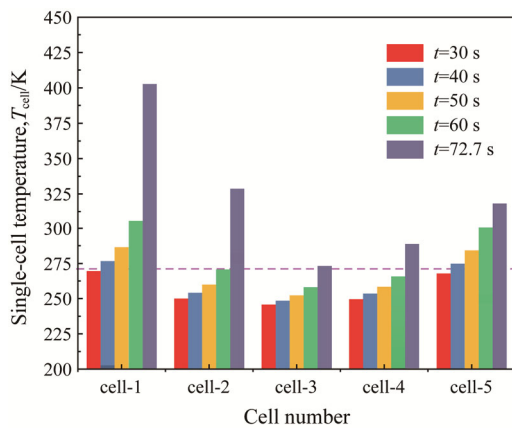


Fig. 11 Variation of the single-cell temperature with start-up time

The impact of the initial current slope on the cold start-up process is shown in Fig. 12. It can be found that the start-up time is decreasing with the increase of the

initial current slope, while the ice volume fraction is rising. When the initial current slope is more significant than $0.7 \text{ A}\cdot\text{s}^{-1}$, the start-up is failed. So, the optimal initial current slope is $0.7 \text{ A}\cdot\text{s}^{-1}$ for the cold start-up of the PEMFC stack.

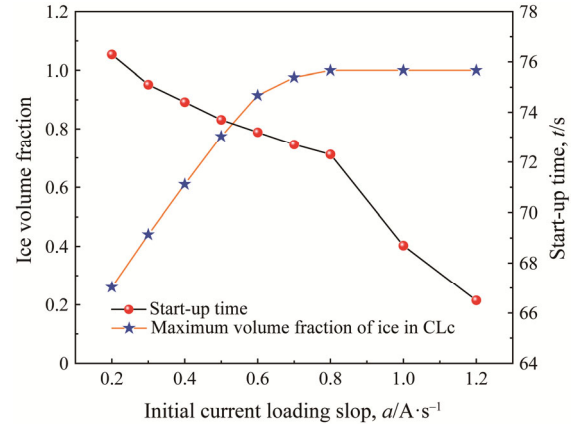


Fig. 12 Variation of maximum ice volume fraction and start-up time with current slope

4. Conclusions

In the present work, a one-dimensional cold start-up model of the PEMFC stack is adopted to explore optimal operating conditions of current and the pre-heating power. The numerical model is validated by comparing the numerical result with the experimental data in the reference. Several initial current slopes and pre-heating power are designed to analyze the effect of the factors on the cold start-up process. Simultaneously, average ice volume fraction, temperature, output voltage, and inner ohmic resistance are comparatively depicted and analyzed. The following conclusions are obtained.

(1) The stack temperature increases continually during the cold start-up process due to the external heating power; thus, the heating power must be small to obtain a lower temperature. The optimal heating power in the studied range is 100 W.

(2) As the initial current slope increases, the current peak value increases during the cold start-up process, and an too-high initial current slope will make the cold start-up process fail. For the problem studied, the optimal initial current slope is $0.7 \text{ A}\cdot\text{s}^{-1}$.

(3) A higher initial current slope will cause a significant inner ohmic resistance. At the initial time, the ohmic resistance is $85 \text{ m}\Omega$. Meanwhile, it changes with the rising of current and start-up time.

(4) The resistance of CLa is the primary part of the total ohmic resistance. For the case study, the resistance percentages in the CLa, MEM, and CLc are approximately 70%, 20%, and 10%, respectively.

Acknowledgment

This work is supported by the key project of NNSFC (51836005), the International Exchange Cooperation Project of NSFC-STINT (5191153015), the Basic research Project of Shaanxi Province (2019ZDXM3-01), the Foundation for Innovative Research Groups of the National Natural Science Foundation of China (51721004) and 111 Project (B16038).

References

- [1] Stolten D., Samsun R.C., Garland N., Fuel cells: data, facts, and figures. Wiley-VCH, DE, 2016.
- [2] Alaswad A., Baroutaji A., Achour H., Carton J., Al Makky A., Olabi A.G., Developments in fuel cell technologies in the transport sector. *International Journal of Hydrogen Energy*, 2016, 41(37): 16499–16508.
- [3] Wang Y., Diaz D.F.R., Chen K.S., Wang Z., Adroher X.C., Materials, technological status, and fundamentals of PEM fuel cells - A review. *Materials Today*, 2020, 32: 178–203.
- [4] Amamou A.A., Kelouwani S., Boulon L., Agbossou K., A comprehensive review of solutions and strategies for cold start of automotive proton exchange membrane fuel cells. *IEEE Access*, 2016, 4: 4989–5002.
- [5] Ichikawa R., Tabe Y., Chikahisa T., Ice formation and current distribution in the catalyst layer of PEM fuel cell at cold start. 11th Polymer Electrolyte Fuel Cell Symposium (PEFC) Under the Auspices of the 220th Meeting of the ECS, Boston, 2011, 41: 733–740.
- [6] Dursch T.J., Trigub G.J., Lujan R., Liu J.F., Mukundan R., Radke C.J., Weber A.Z., Ice-crystallization kinetics in the catalyst layer of a proton-exchange-membrane fuel cell. *Journal of the Electrochemical Society*, 2013, 161(3): F199-F207.
- [7] He P., Chen L., Mu Y.T., Tao W.Q., Lattice Boltzmann method simulation of ice melting process in the gas diffusion layer of fuel cell. *International Journal of Heat and Mass Transfer*, 2020, 149: 119121.
- [8] Wang G.J., Yu Y., Liu H., Gong C.L., Wen S., Wang X.H., Tu Z.K., Progress on design and development of polymer electrolyte membrane fuel cell systems for vehicle applications: A review. *Fuel Processing Technology*, 2018, 179: 203–228.
- [9] Lü X., Qu Y., Wang Y., Qin C., Liu G., A comprehensive review on hybrid power system for PEMFC-HEV: Issues and strategies. *Energy Conversion and Management*, 2018, 171: 1273–1291.
- [10] Jiang F.M., Wang C.Y., Chen K.S., Current ramping: A strategy for rapid start-up of PEMFCs from subfreezing environment. *Journal of the Electrochemical Society*, 2010, 157(3): B342-B347.
- [11] Gwak G., Ju H., A rapid start-up strategy for polymer electrolyte fuel cells at subzero temperatures based on control of the operating current density. *International Journal of Hydrogen Energy*, 2015, 40(35): 11989–11997.
- [12] Jia F., Guo L.J., Liu H.T., A study on current overshoot during start-ups and optimal start-up strategy of proton exchange membrane fuel cells. *International Journal of Hydrogen Energy*, 2015, 40(24): 7754–7761.
- [13] Amamou A., Boulon L., Kelouwani S., An adaptive cold start strategy of proton exchange membrane fuel cell based on maximum power mode. 2019 IEEE Vehicle Power and Propulsion Conference (VPPC), IEEE, 2019, pp. 1–7. DOI: 10.1109/VPPC46532.2019.8952448.
- [14] Liu P., Xu S., A progress review on heating methods and influence factors of cold start for automotive PEMFC system. SAE Technical Paper Series, 2020. DOI: 10.4271/2020-01-0852.
- [15] Meng H., Numerical investigation of transient responses of a PEM fuel cell using a two-phase non-isothermal mixed-domain model. *Journal of Power Sources*, 2007, 171(2): 738–746.
- [16] Luo Y.Q., Jiao K., Jia B., Elucidating the constant power, current and voltage cold start modes of proton exchange membrane fuel cell. *International Journal of Heat and Mass Transfer*, 2014, 77: 489–500.
- [17] Yang Y.B., Ma T.C., Du B.Y., Lin W.K., Yao N.Y., Investigation on the operating conditions of proton exchange membrane fuel cell based on constant voltage cold start mode. *Energies*, 2021, 14(3): 660.
- [18] Amamou A., Kandidayeni M., Macias A., Boulon L., Kelouwani S., Efficient model selection for real-time adaptive cold start strategy of a fuel cell system on vehicular applications. *International Journal of Hydrogen Energy*, 2020, 45(38): 19664–19675.
- [19] Amamou A., Kandidayeni M., Boulon L., Kelouwani S., Real time adaptive efficient cold start strategy for proton exchange membrane fuel cells. *Applied Energy*, 2018, 216: 21–30.
- [20] Luo Y.Q., Jia B., Jiao K., Du Q., Yin Y., Wang H.Z., Xuan J., Catalytic hydrogen-oxygen reaction in anode and cathode for cold start of proton exchange membrane fuel cell. *International Journal of Hydrogen Energy*, 2015, 40(32): 10293–10307.
- [21] Yang Z.R., Jiao K., Wu K.C., Shi W.L., Jiang S.F., Zhang L.H., Du Q., Numerical investigations of assisted heating cold start strategies for proton exchange membrane fuel cell systems. *Energy*, 2021, 222: 119910.
- [22] Tajiri K., Tabuchi Y., Kagami F., Takahashi S., Yoshizawa K., Wang C.Y., Effects of operating and design parameters on PEFC cold start. *Journal of Power Sources*, 2007, 165(1): 279–286.
- [23] Lei L., He P., He P., Tao W.Q., A comparative study: The effect of current loading modes on the cold start-up

- process of PEMFC stack. *Energy Conversion and Management*, 2022, 251: 114991.
- [24] Zhou Y.B., Luo Y.Q., Yu S.H., Jiao K., Modeling of cold start processes and performance optimization for proton exchange membrane fuel cell stacks. *Journal of Power Sources*, 2014, 247: 738–748.
- [25] Du Q., Jia B., Luo Y.Q., Chen J.X., Zhou Y.B., Jiao K., Maximum power cold start mode of proton exchange membrane fuel cell. *International Journal of Hydrogen Energy*, 2014, 39(16): 8390–8400.
- [26] Zang L.F., Hao L., Numerical study of the cold-start process of PEM fuel cells with different current density operating modes. *Journal of Energy Engineering*, 2020, 146(6): 04020057.
- [27] Huo S., Jiao K., Park J.W., On the water transport behavior and phase transition mechanisms in cold start operation of PEM fuel cell. *Applied Energy*, 2019, 233: 776–788.
- [28] Jiao K., Li X.G., Water transport in polymer electrolyte membrane fuel cells. *Progress in Energy and Combustion Science*, 2011, 37(3): 221–291.
- [29] Ye Q., Van Nguyen T., Three-dimensional simulation of liquid water distribution in a PEMFC with experimentally measured capillary functions. *Journal of the Electrochemical Society*, 2007, 154(12): B1242-B1251.
- [30] Springer T.E., Zawodzinski T.A., Gottesfeld S., Polymer electrolyte fuel-cell model. *Journal of the Electrochemical Society*, 1991, 138(8): 2334–2342.
- [31] Kulikovskiy A.A., *Analytical modelling of fuel cells*, first edition ed., Elsevier, UK, 2010.
- [32] Jiao K., Li X.G., Effects of various operating and initial conditions on cold start performance of polymer electrolyte membrane fuel cells. *International Journal of Hydrogen Energy*, 2009, 34(19): 8171–8184.
- [33] Yesilyurt S., Siegel J.B., Stefanopoulou A.G., Modeling and experiments of voltage transients of polymer electrolyte membrane fuel cells with the dead-ended anode. *Journal of Fuel Cell Science and Technology*, 2012, 9(2): 021012.
- [34] Ko J., Ju H., Comparison of numerical simulation results and experimental data during cold-start of polymer electrolyte fuel cells. *Applied Energy*, 2012, 94: 364–374.